Electronic Self-Passivation of Single Vacancy in Black Phosphorus via Ionization

Hanyan Fang[1,†] Aurelio Gallardo[2,3,†] Dikshant Dulal[4] Zhizhan Qiu[1] Jie Su[1] Mykola Telychko[1]
Harshitra Mahalingam[4] Pin Lyu[1] Yixuan Han[1] Yi Zheng[5] Yongqing Cai[6]
Aleksandr Rodin[4,7,*] Pavel Jelínek[2,8,*] and Jiong Lu[1,7,*]

[1]*Department of Chemistry, National University of Singapore, Singapore 117543, Singapore*
[2]*Institute of Physics, Academy of Sciences of the Czech Republic, Prague 162 00, Czech Republic*
[3]*Department of Condensed Matter Physics, Faculty of Mathematics and Physics, Charles University,*
V Holešovičkách 2, Prague 180 00, Czech Republic
[4]*Yale-NUS College, 16 College Avenue West, Singapore 138527, Singapore*
[5]*Zhejiang Province Key Laboratory of Quantum Technology and Device, Department of Physics, Zhejiang University,*
Hangzhou 312007, China
[6]*Joint Key Laboratory of Ministry of Education, Institute of Applied Physics and Materials Engineering,*
University of Macau, Taipa, Macau 999078, China
[7]*Centre for Advanced 2D Materials (CA2DM), National University of Singapore, Singapore 117543, Singapore*
[8]*Regional Centre of Advanced Technologies and Materials, Czech Advanced Technology and Research Institute (CATRIN),*
Palacký University Olomouc, Olomouc 78371, Czech Republic

We report that monoelemental black phosphorus presents a new electronic self-passivation scheme of single vacancy (SV). By means of low-temperature scanning tunneling microscopy and noncontact atomic force microscopy, we demonstrate that the local reconstruction and ionization of SV into negatively charged SV$^-$ leads to the passivation of dangling bonds and, thus, the quenching of in-gap states, which can be achieved by mild thermal annealing or STM tip manipulation. SV exhibits a strong and symmetric Friedel oscillation (FO) pattern, while SV$^-$ shows an asymmetric FO pattern with local perturbation amplitude reduced by one order of magnitude and a faster decay rate. The enhanced passivation by forming SV$^-$ can be attributed to its weak dipolelike perturbation, consistent with density-functional theory numerical calculations. Therefore, self-passivated SV$^-$ is electrically benign and acts as a much weaker scattering center, which may hold the key to further enhance the charge mobility of black phosphorus and its analogs.

High-mobility two-dimensional (2D) semiconductors are essential for the development of ultrathin high-speed and energy-efficient electronics and optoelectronics [1–5]. The intrinsic mobility of defect-free 2D semiconductors is normally set by the effective mass of carriers and phonon scattering processes [6,7]. However, materials synthesis and device fabrication processes of 2D semiconductors, including metal chalcogenides and black phosphorus (BP), inevitably introduce surface vacancies with dangling bonds due to the volatile nature of chalcogen and phosphorus (P) atoms [8–11]. Such atomic defects often act as undesirable sinks for charge carriers and nonradiative recombination centers of photoexcited electron-hole pairs [12–14], which becomes one of the major device performance-limiting factors. Therefore, effective passivation of vacancies in high-mobility 2D semiconductors is vital to maintaining their high-performance device characteristics.

The ideal surface passivation method should deactivate only the defect states without a permanent crystal lattice change and degradation of their electronic performance. Inspired by the conventional passivation technologies used in the semiconductor industry, various strategies, including chemical functionalization [7,15] and surface coating [16,17], have been exploited for the passivation of surface vacancies in 2D semiconductors to remove the associated detrimental in-gap electronic states. However, most passivation schemes developed to date mainly improve the photoluminescence quantum yield without significant enhancement in charge transport properties [15,18] and even degrade the electronic performance by altering the van der Waals structure [16,19].

Here, we demonstrate that monoelemental BP, a prototypical high-mobility 2D semiconductor with a unique puckered square lattice [1,20–25], is able to effectively passivate isolated vacancies by a self-driven lattice reconstruction process to form negatively charged single vacancy (SV$^-$) sites. Such an self-passivation mechanism of vacancies and the associated in-gap electronic states relies on the formation of homoelemental hypervalent bonding, which is not reported in heteroelemental 2D semiconductors (e.g., metal chalcogenides).

As illustrated in Fig. 1(a), removal of one P atom from the buckled lattice in BP creates an SV and leaves dangling

bonds at three adjacent P sites. Neutral SVs in BP with in-gap electronic states were captured by dI/dV measurements [11,26], which play an essential role in modulating electronic and optical properties of BP and, thus, affecting their device characteristics [27–31]. Despite advances in BP research, the atomic-scale structural and electronic properties of SVs and their impact on charge dynamics in BP remain elusive. In addition, the microscopic knowledge of a defect passivation mechanism for eliminating dangling bonds in SVs of BP is still missing.

To this end, we have exploited low-temperature scanning tunneling microscopy (STM) and noncontact atomic force microscopy (nc-AFM) to probe the electronic self-passivation of intrinsic SV in BP at the atomic scale and its role on mobility of the BP field-effect transistor (FET). The versatile bond configuration of P atoms and monoelemental composition of BP introduce a new deactivation mechanism of SV via local reconstruction, saturating the dangling bonds at adjacent P sites. The structural transformation and migration of SV in BP can proceed readily due to a relatively low-energy barrier [32,33]. Among various SV configurations predicted previously [34–38], this one involves the formation of hypervalent four-coordinated P atoms at the defect center [Fig. 1(b)], allowing for the saturation of all the dangling bonds but leaving one extra electron at SV sites (denoted as negatively charged SV⁻). The lattice flexibility of BP ensures a feasible transformation of SVs into electrically inactive ones via self-passivation, which can be triggered by a mild thermal annealing or tip-induced local ionization.
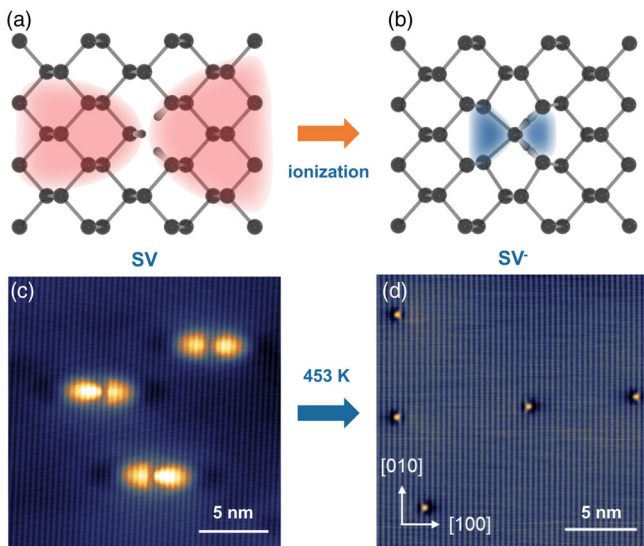

FIG. 1. Thermally driven self-passivation of SV into **SV⁻** via local reconstruction and ionization. (a),(b) Schematics highlight unsaturated SV with dangling bonds and self-passivated (SV⁻), respectively. (c),(d) STM images of BP surface taken before and after the thermal annealing at 453 K followed by rapid cooling. The crystallographic directions are indicated in (d). STM set points: $V_S = -1.0$ V and $I = 0.3$ nA.

STM imaging of BP surface cleaved *in situ* reveals a ubiquitous presence of defects with large-sized dumbbell-shaped appearance across more than tens of zigzag lattice chains [Fig. 1(c)], which are tentatively labeled as neutral SV (in the following context, SV represents neutral SV unless stated otherwise). The spatially extended dumbbell feature is probably associated with the delocalized bound hole states over SV due to its shallow acceptor nature. STM contrast of such defects is gradually reduced as they move away from the top surface (Fig. S5 [39]). We also performed constant-height nc-AFM imaging of these defects with a CO-functionalized tip to monitor the spatial variation of frequency shift (df) in the Pauli repulsive regime [40]. The nc-AFM image of SV shows the perfect zigzag chains attributed to the P atoms at the topmost surface (Fig. S6 [39]). This result suggests that some SVs reside in the subsurface layers, consistent with a recent density-functional theory (DFT) prediction that SVs in the subsurface layers are energetically more favorable [38].

Upon thermal annealing at 453 K followed by rapid cooling, the majority of these dumbbell-shaped SVs vanished. Instead, a new type of defect manifested as a much smaller protrusion predominates the surface [Fig. 1(d)]. A close examination revealed that this new defect adopts a butterfly-shaped feature spanning over two nearest neighboring zigzag chains [Fig. 2(a)]. Moreover, the identical STM contrast of these butterfly-shaped defects suggests that these surface features are due to the reconstruction and migration of SVs during thermal annealing.

To decipher the local structure of butterfly-shaped defects, we performed nc-AFM imaging with a CO-functionalized tip [Fig. 2(c)]. The df image collected by nc-AFM reveals a dark holelike feature surrounded by two bright spots and two dimmer spots. The protrusions in the nc-AFM image correspond to P atom positions due to their stronger repulsive interaction with the CO tip. Therefore, the nc-AFM image suggests the butterfly-shaped defect likely contains a missing top P atom (SV) or both top P and its bonded P atom at the bottom (divacancy denoted as DV). By DFT simulation of various defect structures via the probe particle model (Fig. S3 [39]), the simulated nc-AFM [Fig. 2(d)] of reconstructed SV reproduces the key features in experimental data well, including bright asymmetric protrusions at its two sides. Therefore, the butterfly-shaped defect is determined to be negatively charged SV (SV⁻). The mirror asymmetry along the zigzag direction in both STM and nc-AFM images of SV⁻ stems from the local reconstruction involving the bonding of the central P atom with four adjacent P atoms [Figs. 2(b) and S4 [39]], forming a hypervalent configuration with one extra negative charge.

Kelvin probe force microscopy (KPFM) was further applied to characterize the local contact potential difference (LCPD) between SV⁻ and the bare BP surface. Figure 2(f) presents the KPFM results acquired right over and ∼2.1 nm
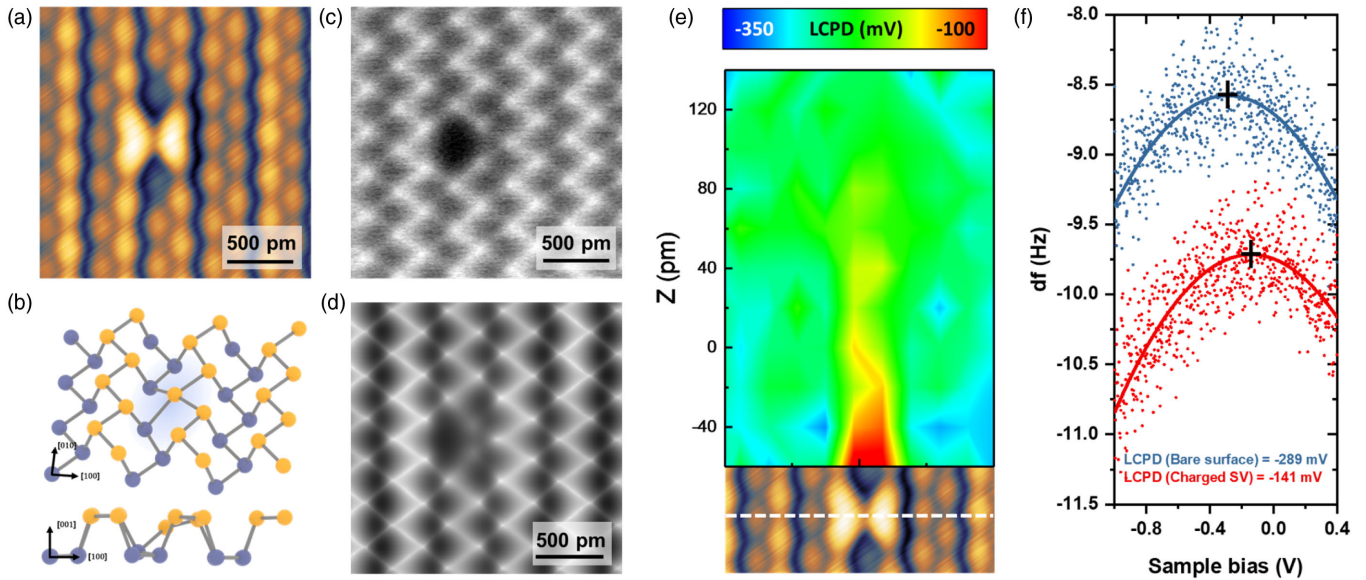
FIG. 2.   Physical characterizations of **SV⁻**. (a) High-resolution STM image of SV⁻ ($V_S = -0.6$ V and $I = 0.3$ nA). (b) Atomic structure for SV⁻ with labeled crystallographic directions and the corresponding side view (bottom panel). The yellow (violet) atoms indicate the P atoms at the top (bottom) sublayers. (c) Atom-resolved nc-AFM image of SV⁻. (d) Simulated nc-AFM image of SV⁻ by the probe particle model. (e) x-z color mapping of spatial-dependent LCPD extracted from KPFM measurements across SV⁻, along the line marked at the bottom of the STM image. (f) Frequency shift (df) measured as a function of the applied sample bias right over and 2.12 nm away from SV⁻ at a relative height of $Z = -40$ pm with respect to the reference point: $Z = 0$ pm ($V_S = -1.0$ V and $I = 50$ pA). Parabolic fits and corresponding parabolic maximum values are indicated in the plot.

away from SV⁻ at a relative height of $Z = -40$ pm. A parabolic fitting of frequency shift $df - V$ curves reveals a positive shift of LCPD (i.e., parabolic maximum) from -289 (over bare BP) to -149 mV (over SV⁻), confirming that SV⁻'s are negatively charged [41]. The LCPD (x, z) color map acquired across SV⁻ along the armchair direction at different tip-sample distances further indicates a smaller LCPD and associated negative charge in close vicinity to SV⁻ [Fig. 2(e)], consistent with the calculated potential profile (Fig. S7 [39]).

Bias-dependent line dI/dV spectra taken across the dumbbell and butterfly defects along the armchair direction (indicated by a white dashed line) are shown in the left panel in Figs. 3(a) and 3(b), respectively. SV mainly induces a strong LDOS modulation in the vicinity of the valence band maximum (VBM) as marked by gray in the right panel in Fig. 3(a). The in-gap states near the valence band (VB) of SV span ≈4 nm away from the defect center, suggesting a shallow acceptor nature forming spatially extended bound hole states [26]. In contrast, SV⁻ lacks in-gap states but exhibits an upward band bending of tens of meV for both VBM and conduction band minimum (CBM). In addition, dI/dV maps taken at 0.4 and -0.1 eV show a weak modulation, including a faint dark depression and protrusion over the defect site, respectively [Figs. 3(e) and 3(f)]. All these observations consistently show that SV⁻ is negatively charged.

The drastically different electronic properties of SV and SV⁻ can be further understood by DFT calculations using the hybrid pbe0 functional. SV shows the spin-polarized density of states (DOS) with in-gap states above the VBM [Fig. 3(c)]. In contrast, the calculated DOS of SV⁻ resembles that of pristine BP (dashed blue curve) with a slight shift of both VB and conduction band (CB) toward each other [Fig. 3(d)]. Upon the local reconstruction and ionization of SV, all the dangling bonds are passivated in SV⁻, eliminating in-gap states and restoring the spin degeneracy in the DOS. A wave function plot of CB and VB band-edge states reveals a major contribution from dispersive bandlike electronic states with small perturbation from the defect (Fig. S9 [39]). In addition, the simulated dI/dV maps at two energetic positions close to the CB [Fig. 3(g)] and VB [Fig. 3(h)] side reproduce the key features in the experimental dI/dV maps well. Therefore, a combination of DFT calculations and nc-AFM imaging unambiguously reveals that butterfly-shaped defects are SV⁻, presumably transformed from neutral SV.

In addition, we took advantage of STM tip manipulation to control the switch between SV and SV⁻ over two individual defects as shown in Fig. S2 [39] (from SV⁻ to SV for defect A and SV to SV⁻ for defect B). We note that a reversible switch over a single defect between SV and SV⁻ is challenging, as high bias applied also may result in pulling nearby P atoms out from the surface, depending on the tip geometry. Nevertheless, positioning the STM tip over one charged defect A(SV⁻) followed by a gradual increase of sample bias to 4.6 V triggers its switch back to
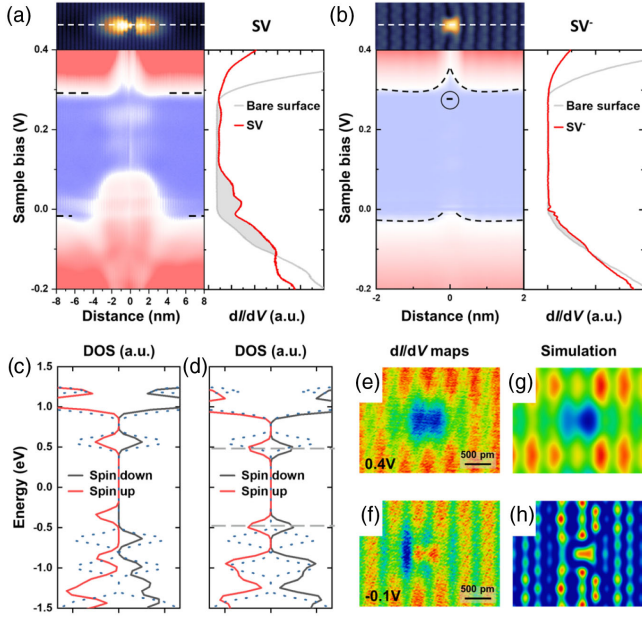
FIG. 3. Electronic structure of **SV⁻**. (a),(b) Color-coded dI/dV spectra taken along armchair direction across SV (a) and SV⁻ (b), where the positions taken for the line spectra are marked by white dashed lines in the corresponding STM images (upper panel). Point dI/dV spectra taken above SV (SV⁻) are compared with the pristine surface in the right panels. (c),(d) Calculated DOS for SV (SV⁻) and pristine BP (indicated by dashed lines). (e),(f) dI/dV maps taken for SV⁻ at $V_S = 0.4$ V and $V_S = -0.1$ V. (g), (h) Simulated dI/dV maps at an energy of 0.47 and -0.47 V, which are indicated by gray dashed lines in (d).

SV with the reemergence of characteristic dumbbell shape and in-gap states (Fig. S2 [39]). Similarly, upon applying a bias of $4.6V$ (Fig. S1 [39]), another defect B(SV) can be transformed into B(SV⁻) with the appearance of butterfly shape and disappearance of in-gap states (Fig. S2 [39]). Such a tip-controlled transformation between SV and SV⁻ is presumably attributed to the ionization and deionization of defects induced by the local electric field or inelastic tunneling process [42,43].

We then evaluated the impact of self-passivation of SV on the carrier mobility of BP FET device (Fig. S15 [39]). After mild annealing with rapid cooling, we observed an increase of hole mobility by 43.0% from saturated mobility ($\sim$325.6 cm^2 V^{-1} s^{-1}) to $\sim$465.7 cm^2 V^{-1} s^{-1} (refer to Supplemental Material [39] for details). These results can be well explained from the local charge scattering behavior by comparing the corresponding Friedel oscillations (FO) before and after ionization of SV. The scattering of charge carriers by defects often produces a periodic long-range modulation of the LDOS with periodicity associated with the wave vector of scattered carriers [44]. We indeed observed a contrasting LDOS oscillation pattern surrounding between SV and SV⁻. The characteristic energy-dependent wavelength of these oscillation patterns verifies their FO origin [Figs. 4(a), 4(b), and
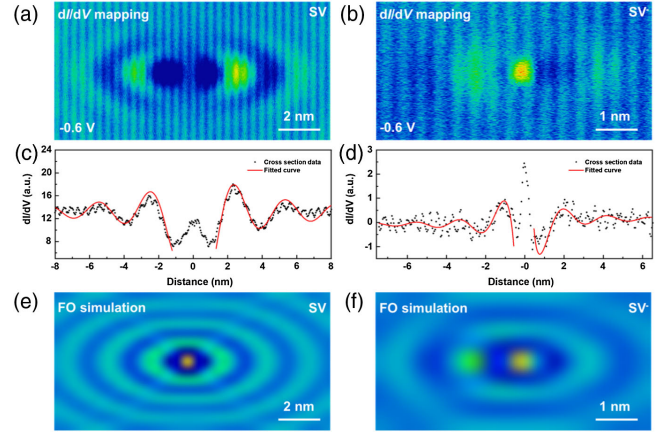

FIG. 4. Probing Friedel oscillations of SV and **SV⁻**. (a),(b) Spatial dI/dV spatial maps taken at $V_S = -0.6$ V for SV and SV⁻, respectively. (c),(d) Cross-section data across the center of SV and SV⁻ along the armchair direction. The fitted curves for FO at both sides of defect are presented in red. Note that the discrepancy in the oscillation wavelength close to the defect center between experiment and theory can be attributed to a strong LDOS modulation at the VB edge of SV that may modify the local bulk bands. (e),(f) Simulated spectral function maps at -0.6 eV for SV and SV⁻, respectively.

S11 [39]). SV exhibits a highly anisotropic FO pattern with a stronger modulation along the armchair direction, which can be attributed to a smaller effective carrier mass along this crystallographic axis [45,46]. According to the standard FO theory [47], we performed the fitting of the line cross-section dI/dV data for both SV and SV⁻ to the expression $A = A_0(\{\cos[2\pi(x - x_c)/\lambda] + \phi\}/(|x - x_c|^r)) + C$, which yields a dramatic difference in the phase, amplitude, and decay rate of FO patterns between SV and SV⁻ [Figs. 4(c) and 4(d)]. First, the fitting of cross-section dI/dV data to the equation above yields a phase difference between the oscillation at two sides of defect by 22.7° for SV and 136.2° for SV⁻. Hence, a small phase shift at SV produces a nearly symmetric FO pattern, while a significant phase shift results in an asymmetric FO pattern across SV⁻. Second, according to the fitting result, the oscillation amplitude in LDOS for SV ($A_L^0 = 8.59$ and $A_R^0 = 11.14$) is nearly one order of magnitude larger than that for SV⁻ ($A_L^- = 1.19$ and $A_R^- = 1.16$). Equally important, SV⁻ shows a faster decay rate (-1.47) than SV (-0.96), which may be the result of a weak perturbation and a large phase shift between two sides of SV⁻.

To understand the origin of different FO behaviors, we performed numerical calculations to simulate FO patterns for both SV and SV⁻ by treating BP as a single (valence) band 2D material with a direction-dependent carrier mass (see Supplemental Material [39] for details). Removing a P atom can be viewed as adding a P "antinucleus." This negatively charged antinucleus creates an attractive long-range potential for the holes, giving rise to FO and midgap

bound states, as seen in Figs. 3(a) and 3(c). Although the potential profile is nontrivial and must include screening effects, it is illuminating to get a rough estimate of the energy scales involved by assuming that the perturbation is limited to the unit cell with the missing P atom. First, we note that the lowest-energy midgap state for SV is located about 0.05 eV above the VBM. Next, following the approach described in Supplemental Material [39], we calculate the spectral function for the unit cell hosting the vacancy for a range of attractive potentials generated by the antinucleus, as shown in Fig. S14 [39]. From our analysis, we observe that the single-unit-cell potential of about -1.5 eV produces a localized state at the correct energy, which is, thus, set as the perturbation potential from SV to calculate the corresponding spectral maps of surrounding BP at different energies. The calculated spectral function map at the energy of -0.6 eV reveals the symmetric oscillation pattern, consistent with experimental dI/dV maps of SV taken at the same energy [Figs. 4(a) and 4(e)]. The FO wavelength of ≈ 2 nm in the armchair direction obtained from the numerical simulations also agrees with the experimental results far from the defect (Fig. S10 [39]). As for SV$^-$, the local reconstruction involving the shift of the central P atom to bond with adjacent four P atoms results in a more diffusive and asymmetric charge density, leading to a dipolelike potential splitting as shown in Fig. S7 [39]. To capture these effects, we split the perturbation (-1.5 eV) from SV into two unit cells. By adjusting the ratio and the separation (Fig. S13 [39]), we found that the calculated spectral function map with a split potential of -1 and -0.5 eV shows the best agreement with the experimental data [Figs. 4(b) and 4(f)]. In fact, the asymmetry and phase shift of spectral function maps is independent on the absolute value of split potentials (Fig. S13 [39]). This points out that making the potential less singular by spreading the perturbation out spatially leads to a reduced band distortion and carrier scattering.

In summary, we demonstrated a new electronic self-passivation of SV in BP through the local reconstruction and ionisation of SV into negatively charged SV$^-$ through a mild thermal annealing or STM tip manipulation, leading to the passivation of all the dangling bonds and elimination of in-gap states. In contrast to SV with a strong and symmetric FO pattern, SV$^-$ shows an asymmetric FO pattern with an oscillation amplitude reduced by one order of magnitude and a faster decay rate, which can be attributed to its weak dipolelike perturbation. Our work opens up a new route for electronic self-passivation of defects, crucial for the further optimization of the carrier mobility in BP and its analogs.

---

[*]Corresponding author.
[†]These authors contributed equally to this work.

[1] L. Li, Y. Yu, G. J. Ye, Q. Ge, X. Ou, H. Wu, D. Feng, X. H. Chen, and Y. Zhang, Nat. Nanotechnol. **9**, 372 (2014).

[2] J. Qiao, X. Kong, Z. X. Hu, F. Yang, and W. Ji, Nat. Commun. **5**, 4475 (2014).

[3] M. Buscema, D. J. Groenendijk, S. I. Blanter, G. A. Steele, H. S. Van Der Zant, and A. Castellanos-Gomez, Nano Lett. **14**, 3347 (2014).

[4] X. Chen, Y. Wu, Z. Wu, Y. Han, S. Xu, L. Wang, W. Ye, T. Han, Y. He, Y. Cai, and N. Wang, Nat. Commun. **6**, 7315 (2015).

[5] F. Sheng, C. Hua, M. Cheng, J. Hu, X. Sun, Q. Tao, H. Lu, Y. Lu, M. Zhong, K. Watanabe, T. Taniguchi, Q. Xia, Z.-A. Xu, and Y. Zheng, Nature (London) **593**, 56 (2021).

[6] J.-H. Chen, C. Jang, S. Xiao, M. Ishigami, and M. S. Fuhrer, Nat. Nanotechnol. **3**, 206 (2008).

[7] Z. Yu, Y. Pan, Y. Shen, Z. Wang, Z. Y. Ong, T. Xu, R. Xin, L. Pan, B. Wang, L. Sun, J. Wang, G. Zhang, Y. W. Zhang, Y. Shi, and X. Wang, Nat. Commun. **5**, 5290 (2014).

[8] Y. C. Lin, T. Björkman, H. P. Komsa, P. Y. Teng, C. H. Yeh, F. S. Huang, K. H. Lin, J. Jadczak, Y. S. Huang, P. W. Chiu, A. V. Krasheninnikov, and K. Suenaga, Nat. Commun. **6**, 6736 (2015).

[9] B. Schuler, D. Y. Qiu, S. Refaely-Abramson, C. Kastl, C. T. Chen, S. Barja, R. J. Koch, D. F. Ogletree, S. Aloni, A. M. Schwartzberg, J. B. Neaton, S. G. Louie, and A. Weber-Bargioni, Phys. Rev. Lett. **123**, 076801 (2019).

[10] Y. Liu, Z. Qiu, A. Carvalho, Y. Bao, H. Xu, S. J. Tan, W. Liu, A. H. Castro Neto, K. P. Loh, and J. Lu, Nano Lett. **17**, 1970 (2017).

[11] B. Kiraly, N. Hauptmann, A. N. Rudenko, M. I. Katsnelson, and A. A. Khajetoorians, Nano Lett. **17**, 3607 (2017).

[12] M. D. Pashley, K. W. Haberern, R. M. Feenstra, and P. D. Kirchner, Phys. Rev. B **48**, 4612 (1993).

[13] J. Hong, Z. Hu, M. Probert, K. Li, D. Lv, X. Yang, L. Gu, N. Mao, Q. Feng, L. Xie, J. Zhang, D. Wu, Z. Zhang, C. Jin, W. Ji, X. Zhang, J. Yuan, and Z. Zhang, Nat. Commun. **6**, 6293 (2015).

[14] M. A. Khan, M. Erementchouk, J. Hendrickson, and M. N. Leuenberger, Phys. Rev. B **95**, 245435 (2017).

[15] H. V. Han, A. Y. Lu, L. S. Lu, J. K. Huang, H. Li, C. L. Hsu, Y. C. Lin, M. H. Chiu, K. Suenaga, C. W. Chu, H. C. Kuo, W. H. Chang, L. J. Li, and Y. Shi, ACS Nano **10**, 1454 (2016).

[16] J. Pak, J. Jang, K. Cho, T.-Y. Kim, J.-K. Kim, Y. Song, W.-K. Hong, M. Min, H. Lee, and T. Lee, Nanoscale **7,** 18780 (2015).

[17] J. H. Park, A. Sanne, Y. Guo, M. Amani, K. Zhang, H. C. Movva, J. A. Robinson, A. Javey, J. Robertson, S. K. Banerjee, and A. C. Kummel, Sci. Adv. **3,** e1701661 (2017).

[18] M. Amani, D.-H. Lien, D. Kiriya, J. Xiao, A. Azcatl, J. Noh, S. R. Madhvapathy, R. Addou, S. KC, M. Dubey, K. Cho, R. M. Wallace, S.-C. Lee, J.-H. He, J. W. Ager, X. Zhang, E. Yablonovitch, and A. Javey, Science **350,** 1065 (2015).

[19] K. Cho, M. Min, T.-Y. Kim, H. Jeong, J. Pak, J.-K. Kim, J. Jang, S. J. Yun, Y. H. Lee, W.-K. Hong, and T. Lee, ACS Nano **9,** 8044 (2015).

[20] Z. Luo, J. Maassen, Y. Deng, Y. Du, R. P. Garrelts, M. S. Lundstrom, P. D. Ye, and X. Xu, Nat. Commun. **6,** 8572 (2015).

[21] L. Li, G. J. Ye, V. Tran, R. Fei, G. Chen, H. Wang, J. Wang, K. Watanabe, T. Taniguchi, L. Yang, X. H. Chen, and Y. Zhang, Nat. Nanotechnol. **10,** 608 (2015).

[22] B. Deng, V. Tran, Y. Xie, H. Jiang, C. Li, Q. Guo, X. Wang, H. Tian, S. J. Koester, H. Wang, J. J. Cha, Q. Xia, L. Yang, and F. Xia, Nat. Commun. **8,** 14474 (2017).

[23] L. Li, J. Kim, C. Jin, G. J. Ye, D. Y. Qiu, F. H. Da Jornada, Z. Shi, L. Chen, Z. Zhang, F. Yang, K. Watanabe, T. Taniguchi, W. Ren, S. G. Louie, X. H. Chen, Y. Zhang, and F. Wang, Nat. Nanotechnol. **12,** 21 (2017).

[24] S. W. Jung, S. H. Ryu, W. J. Shin, Y. Sohn, M. Huh, R. J. Koch, C. Jozwiak, E. Rotenberg, A. Bostwick, and K. S. Kim, Nat. Mater. **19,** 277 (2020).

[25] G. Long, D. Maryenko, J. Shen, S. Xu, J. Hou, Z. Wu, W. K. Wong, T. Han, J. Lin, Y. Cai, R. Lortz, and N. Wang, Nano Lett. **16,** 7768 (2016).

[26] Z. Qiu, H. Fang, A. Carvalho, A. S. Rodin, Y. Liu, S. J. Tan, M. Telychko, P. Lv, J. Su, Y. Wang, A. H. Castro Neto, and J. Lu, Nano Lett. **17,** 6935 (2017).

[27] F. Xia, H. Wang, and Y. Jia, Nat. Commun. **5,** 4458 (2014).

[28] X. Wang, A. M. Jones, K. L. Seyler, V. Tran, Y. Jia, H. Zhao, H. Wang, L. Yang, X. Xu, and F. Xia, Nat. Nanotechnol. **10,** 517 (2015).

[29] Y. Liu, T. Low, and P. P. Ruden, Phys. Rev. B **93,** 165402 (2016).

[30] J. V. Riffle, C. Flynn, B. St Laurent, C. A. Ayotte, C. A. Caputo, and S. M. Hollen, J. Appl. Phys. **123,** 044301 (2018).

[31] R. Babar and M. Kabir, Phys. Rev. Mater. **3,** 074008 (2019).

[32] Y. Cai, Q. Ke, G. Zhang, B. I. Yakobson, and Y.-W. Zhang, J. Am. Chem. Soc. **138,** 10199 (2016).

[33] F. Yao, Y. Cai, Z. Xiao, G. Zhang, R.-J. Xie, and C. Jin, 2D Mater. **8,** 025004 (2021).

[34] Y. Liu, F. Xu, Z. Zhang, E. S. Penev, and B. I. Yakobson, Nano Lett. **14,** 6782 (2014).

[35] Y. Guo and J. Robertson, Sci. Rep. **5,** 14165 (2015).

[36] T. Hu and J. Dong, Nanotechnology **26,** 065705 (2015).

[37] W. Hu and J. Yang, J. Phys. Chem. C **119,** 20474 (2015).

[38] J. Gaberle and A. L. Shluger, Nanoscale **10,** 19536 (2018).

[39] See Supplemental Material at http://link.aps.org/supplemental/10.1103/PhysRevLett.128.176801 for sample preparation, simulation methods and other related details.

[40] L. Gross, F. Mohn, N. Moll, P. Liljeroth, and G. Meyer, Science **325,** 1110 (2009).

[41] L. Gross, F. Mohn, P. Liljeroth, J. Repp, F. J. Giessible, and G. Meyer, Science **324,** 1428 (2009).

[42] D. H. Lee and J. A. Gupta, Science **330,** 1807 (2010).

[43] D. Wong, J. Velasco, L. Ju, J. Lee, S. Kahn, H. Z. Tsai, C. Germany, T. Taniguchi, K. Watanabe, A. Zettl, F. Wang, and M. F. Crommie, Nat. Nanotechnol. **10,** 949 (2015).

[44] J. Friedel, Lond. Edinb. Dublin Philos. Mag. J. Sci. **43,** 153 (1952).

[45] Y. L. Zou, J. Song, C. Bai, and K. Chang, Phys. Rev. B **94,** 035431 (2016).

[46] B. Kiraly, E. J. Knol, K. Volckaert, D. Biswas, A. N. Rudenko, D. A. Prishchenko, V. G. Mazurenko, M. I. Katsnelson, P. Hofmann, D. Wegner, and A. A. Khajetoorians, Phys. Rev. Lett. **123,** 216403 (2019).

[47] M. F. Crommie, C. P. Lutz, and D. M. Eigler, Nature (London) **363,** 524 (1993).